Molecular structure and vibrational spectroscopic investigation of 4-chloro-4′dimethylamino-benzylidene aniline using density functional theory

ARTICLE *in* JOURNAL OF MOLECULAR STRUCTURE · SEPTEMBER 2010

Impact Factor: 1.6 · DOI: 10.1016/j.molstruc.2010.07.003

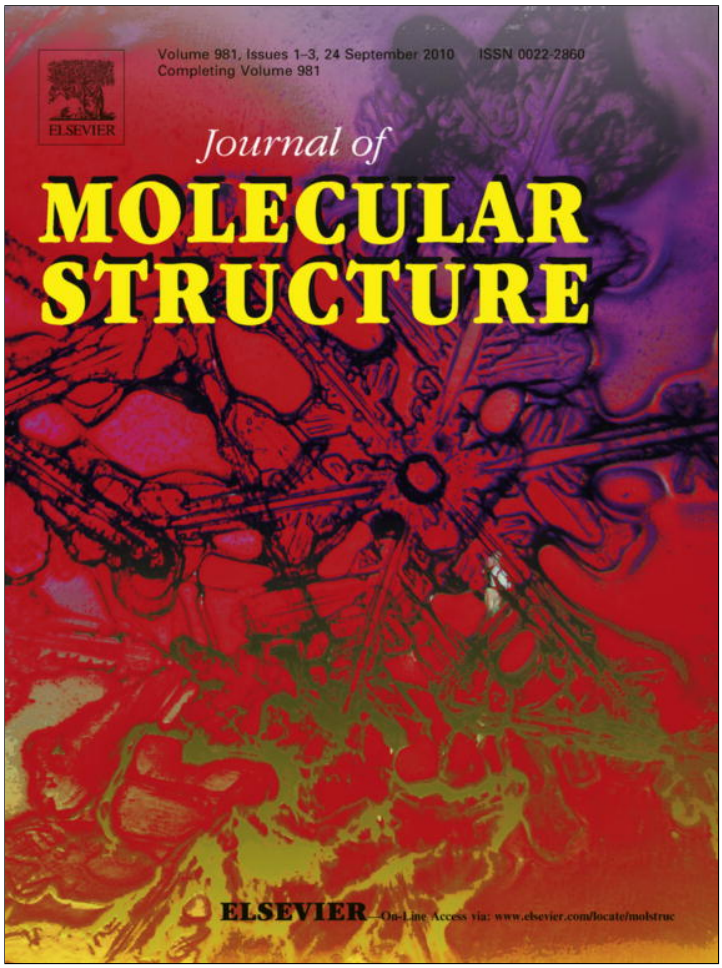

Journal of Molecular Structure 981 (2010) 1–9

Contents lists available at ScienceDirect

Journal of Molecular Structure

journal homepage: www.elsevier.com/locate/molstruc

Molecular structure and vibrational spectroscopic investigation of 4-chloro-4′dimethylamino-benzylidene aniline using density functional theory

Sapna Pathak [a], Anuj Kumar [a,*], Poonam Tandon [b]

[a] Department of Physics, Jaypee University of Engineering and Technology, Raghogarh, Guna 473 226, India
[b] Department of Physics, University of Lucknow, Lucknow 226 007, India

ARTICLE INFO

Article history:
Received 22 April 2010
Received in revised form 10 June 2010
Accepted 5 July 2010
Available online 8 July 2010

Keywords:
Non-linear optical crystal
Vibrational analysis
DFT
NBO

ABSTRACT

The Fourier Transform Raman and infrared spectra of the crystallized 4-chloro-4′dimethylamino-benzylidine aniline (CDMABA) have been recorded in the region 3500–200 cm^{-1} and 4000–400 cm^{-1}, respectively. The geometry optimization, electrostatic potential surface and vibrational wavenumbers with Raman scattering activities and infrared absorption intensities have been investigated by density functional theory (DFT) method using 6-311++G(d,p) basis set and Becke's three-parameters hybrid functional (B3LYP). The calculated molecular geometry has been compared with the experimental data obtained from XRD. The assignments of the vibrational spectra have been carried out with the aid of normal coordinate analysis (NCA). The natural bond orbital analysis (NBO) has been performed in order to study the intramolecular bonding, interactions among bonds and delocalization of unpaired electrons. The electrostatic potential surface mapped with isodensity surface has been obtained.

1. Introduction

Non-linear optical (NLO) materials with high optical nonlinearities have been the subject of intense research in the last few years. These materials have potential applications in harmonic generation, amplitude and phase modulation, switching and other optical signal processing devices [1–3]. Molecules with large third order non-linear optical properties can be incorporated in devices used for applications in optical disk data storage, optical high-speed information processing, optical communications, optoelectronics, optical computing, optical logic gates, laser radiation protection, locked laser mode, laser fusion reactions, laser remote sensing, color display, medical diagnostics, etc. [4–7]. Now a days, NLO organic crystals are competing with widely used inorganic materials because their preparation is less expensive, non-linear susceptibilities are high, their large birefringence to use as frequency converters and laser damage thresholds are fairly high.

Among organic crystals for NLO applications, Schiff bases display specific features of interest such as relatively large molecular hyperpolarizabilities due to the presence of delocalized π-electron systems connecting donor and acceptor groups [8]. Organic compounds obtained by condensation of primary amines with aldehydes or ketones yield Schiff bases containing imine (C=N) function group [9]. Some of them may have a variety of substituents with electron-donor or electron-acceptor groups, which conform conjugated π-electron systems and show a large second order optical nonlinearities such as 4-nitro-4′-methyl benzylidene aniline(NMBA) [10], 4-nitro-4′-methoxy benzylidene aniline(NMOBA) [11]. Benzylidene anilines constitute an important class of Schiff bases that have been widely used in coordinate, medical and biological chemistry. They posses significant anticancer anti-inflammatory activities and may also serve as reagents for stereo selective organic synthesis [12]. Recently, the thermocromism, photochromism and non-linear optical responses of the Schiff base compounds find applications in modern technologies.

4-chloro-4′dimethylamino-benzylidine aniline (CDMABA) is a new benzylidine aniline derivative which shows a large third order non-linear absorption. Single crystal structure determinations showed that CDMABA belongs to a monoclinic system, space group $P2_1/c$ with cell parameters $a = 9.852$ (6) Å, $b = 16.268$ (9) Å, $c = 9.512$ (6) Å, and $\beta = 119.904$ (6)° [13].The structure of CDMABA crystal is of much interest, as these crystals do not contains any strong-hydrogen-bond-forming groups, such as –COOH, $–NH_2CO–$ or $–NO_2$ therefore various weak interactions, such as C–H···π [14], π–π [15] and weak hydrogen-bonding interactions, and the interplay between these interactions play an important role in determining conformation of molecule.

Infrared and Raman spectroscopies are among the traditional methods of analysis, and particularly powerful for nondestructive characterization of substances including living material. For complete understanding of the vibrational spectra, we report a normal-mode analysis of CDMABA by combining Raman and infrared data using density functional theory. In the present work,

* Corresponding author. Tel.: +91 7544 267051; fax: +91 7544 267011.
E-mail addresses: anuj.kumar@jiet.ac.in, anujkumar.jiet@gmail.com (A. Kumar).

0022-2860/$ - see front matter © 2010 Elsevier B.V. All rights reserved.
doi:10.1016/j.molstruc.2010.07.003

quantum mechanical calculations have been used in order to investigate conformational stability of the CDMABA molecule. Geometry optimizations of the possible stable rotamers were performed, and the corresponding relative energies were compared. We have calculated the equilibrium geometry, harmonic vibrational wavenumbers, electrostatic potential surfaces, absolute Raman scattering activities and infrared absorption intensities by DFT with B3LYP functionals having extended basis set 6-311++G(d,p). Optimized geometry obtained by DFT method, compares well with reported X-ray data (Fig. 1a), is shown in Fig. 1b. The calculated vibrational spectra were analyzed on the basis of the potential energy distribution (PED) of each vibrational mode, which allowed us to obtain a quantitative as well as qualitative interpretation of the infrared and Raman spectra.

2. Spectral measurements

Transparent crystals of dimension 8 mm × 5 mm × 4 mm of CDMABA was obtained from Dr. K. Ramamurthi of Crystal Growth and Thin Film Laboratory, School of Physics, Bharathidasan University, Tiruchirappalli 620 024, Tamil Nadu, India [16].

2.1. Fourier Transform Infrared Spectroscopy

Fourier Transform Infrared Spectra were recorded in the range 4000–400 cm^{-1}, on Bruker Tensor 27 FT-IR spectrometer by KBr pellet technique using 100 scans with a spectral resolution of 4 cm^{-1}.

2.2. Fourier Transform Raman Spectroscopy

FT-Raman spectra were measured using Perkin–Elmer 2000R spectrometer with a resolution of 4 cm^{-1}. This spectrometer is equipped with 1064 nm Nd: YAG laser with an output power of about 100 mw at the sample position. The upper limit for the Raman wavenumber was restricted to 3500 cm^{-1} and lower to 200 cm^{-1}.

3. Computational details

Calculations for electronic structure and geometry optimization of the stable conformers of the molecule were done by DFT [17] using the Gaussian 03 program [18] package employing 6-311++G(d,p) basis sets and Becke's three parameter (local, non-local, Hartree–Fock) hybrid exchange functionals with Lee–Yang–Parr correlation functionals (B3LYP) [19–21]. The absolute Raman intensities and infrared absorption intensities were calculated in the harmonic approximation, at the same level of theory as used for the optimized geometries, from the derivatives of the dipole moment and polarizability of each normal mode, respectively. The normal-mode analysis was employed to calculate PED for each of the internal coordinates using localized symmetry [22,23]. For this purpose a complete set of 93 internal coordinates was defined using Pulay's recommendations [22,23]. The vibrational assignments of the normal modes were proposed on the basis of the PED calculated using the program GAR2PED [24]. Raman and infrared spectra were simulated using a pure Lorentzian band profile (fwhm = 10 cm^{-1}). Visualization and confirmation of the calculated forms of the vibrations were done using the CHEMCRAFT program [25].

Calculated DFT vibrational wavenumbers are known to be higher than the experimental wavenumbers as the anharmonicity effects are neglected. Therefore, wavenumbers obtained by DFT were scaled down by the wavenumber linear scaling procedure (WLS) $\nu_{obs} = (1.0087–0.0000163\nu_{calc.})\nu_{calc.}$ cm^{-1} [26]. The WLS method using this relationship predicts vibrational wavenumbers with high accuracy and is applicable to a large number of compounds, except for those where the effect of dispersion forces is significant. All the calculated vibrational wavenumbers reported in this study are the scaled values.

The natural bonding orbitals (NBO) analysis has been performed in order to investigate intramolecular charge transfer interactions, rehybridization and delocalization of electron density within the molecule. The main natural orbital interactions were analyzed on the basis of NBO calculations done at DFT/B3LYP level using NBO 5.0 program as implemented in Gaussian 03 package. In the NBO analysis [27,28] the electronic wave functions are interpreted in terms of a set of occupied Lewis-type (bond or lone pair) and a set of unoccupied non-Lewis (antibond or rydberg) localized NBO orbitals. Delocalization of electron density (ED) between these orbitals corresponds to a stabilizing donor–acceptor interaction. The second-order perturbation theory has been employed to evaluate the stabilization energies of all possible interactions between donor and acceptor orbitals in the NBO basis. The interactions result in a loss of occupancy from the localized NBO of the idealized Lewis structure into an empty non-Lewis orbital. The delocalization effects (or donor–acceptor charge transfers (CTs)) can be estimated from off-diagonal elements of the Fock matrix in the NBO basis. For each donor (i) and acceptor (j), the stabilization energy $E(2)$ associated with the delocalization $i \rightarrow j$ is estimated as

$$E^{(2)} = \Delta E_{ij} = q_i \frac{F(i,j)^2}{\varepsilon_j - \varepsilon_i} \quad (1)$$

where q_i is the donor orbital occupancy, ε_i and ε_j are diagonal elements and $F(i,j)$ is the off diagonal NBO Fock or Kohn–Sham matrix element [27].

4. Results and discussion

4.1. Geometry optimization and energies

Geometry of CDMABA conformation was optimized without any constraint to the potential energy surface using given X-ray diffraction data as initial point [13]. All the estimated bond lengths

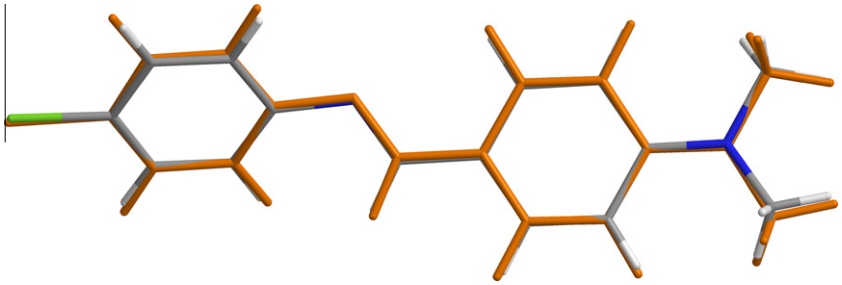

Fig. 1a. Comparison of optimized geometry with geometry obtained by single crystal XRD.

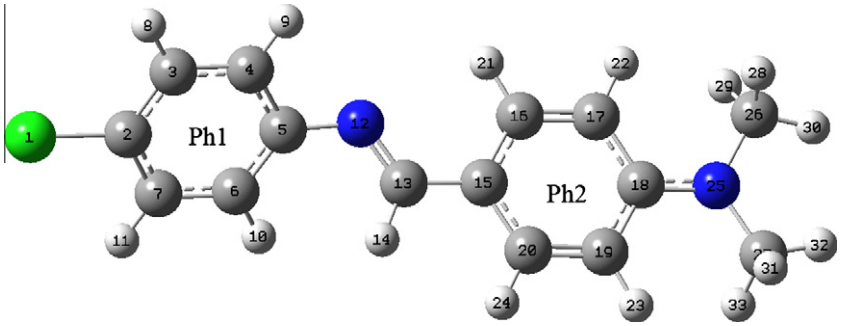

Fig. 1b. Optimized structure of CDMABA.

Table 1
Optimized geometrical parameters of CDMABA by DFT in comparison with XRD data.

Geometrical parameters	Optimized (B3LYP)	XRD	Geometrical parameters	Optimized (B3LYP)	XRD
Cl1–C2	1.762	1.744	C7–C6–H	119.3	119.8
C2–C3	1.393	1.386	C6–C7–H	120.5	120.3
C2–C7	1.390	1.379	N12–C13–H	121.1	118.9
C3–C4	1.389	1.379	N12–C13–C15	123.6	122.3
C3–H	1.083	0.951	H–C13–C15	115.3	118.8
C4–C5	1.404	1.393	C13–C15–C16	122.4	122.3
C4–H	1.083	0.950	C13–C15–C20	120.1	120.4
C5–C6	1.405	1.393	C16–C15–C20	117.6	117.3
C5–N12	1.402	1.416	C15–C16–C17	121.4	121.8
C6–C7	1.392	1.384	C15–C16–H	118.6	119.1
C6–H	1.084	0.950	C15–C20–C19	121.8	121.9
C7–H	1.083	0.951	C15–C20–H	119.3	119.0
N12–C13	1.281	1.280	C17–C16–H	120.0	119.1
C13–H	1.100	0.950	C16–C17–C18	121.2	121.1
C13–C15	1.456	1.452	C16–C17–H	118.7	119.5
C15–C16	1.405	1.397	C18–C17–H	120.2	119.4
C15–C20	1.402	1.397	C17–C18–C19	117.3	116.9
C16–C17	1.381	1.371	C17–C18–N25	121.2	121.2
C16–H	1.084	0.950	C19–C18–N25	121.5	121.9
C17–C18	1.419	1.419	C18–C19–C20	120.7	120.9
C17–H	1.081	0.949	C18–C19–H	120.5	119.6
C18–C19	1.414	1.411	C18–N25–C26	120.1	120.9
C18–N25	1.379	1.366	C18–N25–C27	120.0	121.4
C19–C20	1.386	1.377	C20–C19–H	118.8	119.5
C19–H	1.081	0.950	C19–C20–H	118.8	119.0
C20–H	1.086	0.950	C26–N25–C27	118.6	116.1
N25–C26	1.455	1.446	N25–C26–H	112.4	109.5
N25–C27	1.455	1.445	N25–C26–H	111.2	109.5
C26–H	1.098	0.980	N25–C26–H	109.0	109.5
C26–H	1.094	0.981	N25–C27–H	112.4	109.5
C26–H	1.089	0.979	N25–C27–H	109.1	109.5
C27–H	1.099	0.980	N25–C27–H	111.2	109.5
C27–H	1.089	0.979	H–C26–H	108.2	109.5
C27–H	1.094	0.980	H–C26–H	108.2	109.5
C1–C2–C3	119.6	119.0	H–C26–H	107.6	109.4
C1–C2–C7	119.5	119.7	H–C27–H	108.2	109.5
C3–C2–C7	120.9	121.3	H–C27–H	108.2	109.5
C2–C3–C4	119.3	118.7	H–C27–H	107.6	109.5
C2–C3–H	120.1	120.6	N12–C5–C6–C7	−178.68	176.86
C2–C7–C6	119.4	119.5	C13–N12–C5–C4	142.023	140.53
C2–C7–H	120.1	120.3	C13–N12–C5–C6	−40.925	43.0
C4–C3–H	120.6	120.6	C5–N12–C13–C15	176.767	179.93
C3–C4–C5	121.0	121.3	C13–C15–C16–C17	179.809	176.70
C3–C4–H	120.4	119.3	C20–C15–C13–N12	177.687	170.00
C5–C4–H	118.6	119.4	C16–C15–C13–N12	−1.915	7.4
C4–C5–C6	118.4	118.8	C13–C15–C20–C19	−179.8	175.78
C4–C5–N12	118.2	117.7	C26–N25–C18–C17	6.98530	0.1
C6–C5–N12	123.3	123.4	C27–N25–C18–C17	173.585	165.29
C5–C6–C7	120.9	120.5	C26–N25–C18–C19	−173.29	179.36
C5–C6–H	119.8	119.8	C27–N25–C18–C19	−6.688	−15.4
C5–N12–C13	120.1	119.4			

and angles of the optimized CDMABA molecule calculated at B3LYP level of theory are listed in Table 1 along with the reported molecular parameters [13].

The DFT calculations provide the trans configuration, at the imine bridge, of the target molecule with a torsional angle of 176.767°. It also predicts the tilting of phenyl ring plane Ph1 to

42.84° with respect to the Ph2 ring plane. This is attributed to the steric hindrance caused due to the van der Waals repulsion between the aryl and aliphatic hydrogen atoms. This is evident from the short intramolecular nonbonded H10···H14, H14···H24 distances: 2.376 Å each. In order to reduce steric repulsion between imine bridge and the phenyl ring, the bond angles C6–C5–N12, C13–C15–C16 have been expanded from the usual values to 123.35°, 122.35°, respectively. The rotation of Ph1 about C5–N12 and Ph2 about C13–C15 bonds at the expense of the conjugation energy of the system is another way to minimize the van der Waals repulsion. The dissimilarities found in the aromatic bond lengths and bond angles in the optimized geometry for both phenyl rings are in agreement with the reported X-ray structure [13]. The aromatic substitution by an electron-donating dimethylamino group at C18 leads to a contraction of the internal angle to 117° and an associated elongation in the bond lengths C17–C18 and C18–C19 to 1.419 and 1.414 Å, respectively. However, the same effect obtained at C5 and C15 are mainly due to the steric effect as discussed above. The other endocyclic angles at the C atoms of Ph2 are larger than 120° so as to offset the narrowing at C5 and C18. The electronic coupling between the amino nitrogen lonepair electrons and the phenyl ring π-system creates phenyl-N conjugation. This phenyl-N conjugation brings about ICT [29] and this leads to superior performance in material chemistry such as hyperpolarizability [30], hole transport [31,32], electroluminescence [32,33], etc. The deviation from the coplanarity of the NC18 moiety with respect to the phenyl ring planes is also an outcome of the optimized geometry, which is reflected in the geometry by their dihedral angles C19–C18–N25–C26 and C19–C18–N25–C27 at −173.288° and −6.688°, respectively.

4.2. Potential energy scan studies

In order to reveal all possible conformations of CDMABA, a detailed two dimensional potential energy scan was performed for the dihedral angles ϕ1(C13–N12–C5–C4) and ϕ2(C16–C15–C13–N12) at the B3LYP/6-31G level of theory. The scan studies was obtained by minimizing the potential energy in all geometrical parameters by varying the torsion angles at a step of 10° in the range of 0–360° rotation around the bond. The variations of the potential energy change from its equilibrium with the torsional perturbation are presented in Fig. 2. The PES scan revealed that the CDMABA molecule has minimum energy at a combination of ϕ 1 = 142° and ϕ2 = −1.9°.

4.3. Natural bond orbital analysis

NBO analysis proves to be an efficient method for study of the intra- and intermolecular bonding and interactions among bonds. It also provides the convenient basis for the interpretation of hyperconjugative interaction and electron density charge transfer from the filled lone pair electrons. The second-order perturbation theory analysis of Fock matrix in NBO basis of CDMABA shows strong intramolecular hyperconjugative interactions. Some important interactions between Lewis and non-Lewis orbitals along with their interacting stabilization energies are presented in Table 2. The larger the $E(2)$ value, the more intensive is the interaction between electron donors and acceptors, i.e. the more electron donating tendency from electron donors to acceptors and the greater the extent of conjugation of the whole system.

The intramolecular hyperconjugative interactions are formed by the orbital overlap between π(C–C) and π*(C–C) bond orbitals which results ICT causing stabilization of the system. These interactions are observed as an increase in electron density (ED) in C–C antibonding orbital that weakens the respective bonds [34]. The ED at the six conjugated π bonds (∼1.6–1.7e) and π* bonds (∼0.3–0.4 e) of the phenyl rings clearly demonstrates strong delocalization leading to stabilization of energy in the range of 13.75–26.06 kcal/mol.

The most important interaction (n → π*), related to the resonance in the molecule, is electron donation from the LP(1)N25 atom of the electron donating group to the antibonding acceptor π*(C18–C19) of the phenyl ring and results the maximum stabilization energy 45.32 kcal/mol due to small energy differences between donor and acceptor. There occurs a strong intramolecular hyperconjugative interaction of lone pair electrons from Cl1 atom to the π*(C2–C7) bond of the phenyl ring leading to the stabilization energy of 11.75 kcal/mol. These enhanced π*(C2–C7) and π*(C18–C19) NBOs further conjugate with π*(C5–C6), π*(C3–C4) and π*(C15–C20), π*(C16–C17), respectively. This results in an

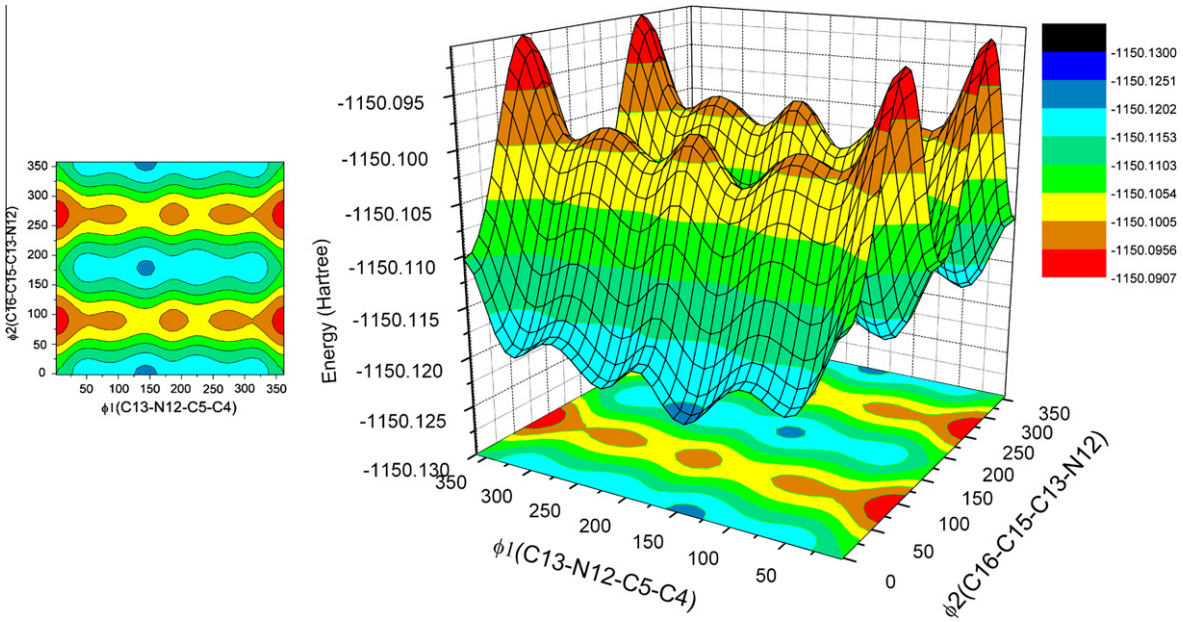

Fig. 2. PES of ϕ1 and ϕ2 of CDMABA. (For interpretation of the references to color in this figure legend, the reader is referred to the web version of the article.)

Table 2
Second-order perturbation theory analysis of Fock matrix in NBO basis.

Donor NBO(i)	ED(i)/e	Acceptor NBO(j)	ED(j)/e	$E^{(2)}$[a] kcal mol^{-1}	$E(j)$–$E(i)$[b] (a.u.)	$F(i,j)$[c] (a.u.)
n3(Cl1)	1.93394	π*C2–C7	0.40176	11.75	0.33	0.061
n1(N12)	1.87762	σ*C5–C6	0.03261	6.38	0.90	0.069
		π*C5–C6	0.38458	5.88	0.36	0.044
		σ*C13–H14	0.04412	12.99	0.72	0.088
n1(N25)	1.71268	π*C18–C19	0.43071	45.32	0.27	0.103
		σ*C26–H28	0.02081	6.82	0.63	0.063
		σ*C27–H31	0.02108	6.88	0.63	0.063
πC3–C4	1.68551	π*C2–C7	0.40176	19.76	0.27	0.067
		π*C5–C6	0.38458	19.7	0.28	0.068
πC5–C6	1.62945	π*C3–C4	0.31387	18.47	0.28	0.066
		π*C2–C7	0.40176	23.64	0.27	0.072
πC2–C7	1.68733	π*C3–C4	0.31387	19.6	0.3	0.068
		π*C5–C6	0.38458	17.01	0.3	0.065
πC16–C17	1.73046	π*C15–C20	0.41301	14.66	0.29	0.06
		π*C18–C19	0.43071	21.55	0.28	0.072
πC15–C20	1.63188	π*C16–C17	0.28232	21.84	0.28	0.072
		π*N12–C13	0.17737	21.21	0.28	0.072
		π*C18–C19	0.43071	17	0.27	0.061
πC18–C19	1.61080	π*C15–C20	0.41301	26.06	0.29	0.077
		π*C16–C17	0.28232	13.75	0.29	0.058
πN12–C13		π*C5–C6	0.38458	10.35	0.35	0.059
		π*C15–C20	0.41301	7.72	0.36	0.051
π*C2–C7	0.40176	π*C5–C6	0.38458	242.13	0.01	0.083
		π*C3–C4	0.31387	183.33	0.02	0.08
π*C18–C19	0.43071	π*C16–C17	0.28232	179.38	0.02	0.079
		π*C15–C20	0.41301	306.3	0.01	0.082

[a] $E^{(2)}$ is the energy of hyperconjugative interactions.
[b] Energy difference between donor and acceptor i and j NBO orbitals.
[c] $F(i,j)$ is the Fock matrix element between i and j NBO orbitals.

enormous stabilization of 242.13, 183.33 kcal/mol and 306.3, 179.38 kcal/mol, respectively. The hyperconjugative interaction (n → σ*) between the electron-donating nitrogen of the imine bridge and antibonding orbitals C5–C6 and C13–H14 give rise to the stabilization energies of 6.38 and 12.99 kcal/mol, respectively. These intramolecular charge transfer (n → σ*, n → π* and π → π*) can induce large nonlinearity in the molecule.

4.4. Molecular electrostatic potential

In CDMABA molecule various weak interactions, such as C–H···π, π–π and weak hydrogen-bonding interactions are manifested and play an important role in determining stability of the molecule. The presence of dimethylamino group leads to the electronic coupling between ring π electrons and nitrogen lone pair electrons which provides stabilization to the molecular structure and enhance its non-linear optical properties. Hence it is of importance to study the electrostatic potential distribution in the molecule.

The molecular electrostatic potential (MEP) is a property that the electrons and nuclei of a molecule create at each point r in the surrounding space [35]. ESP serves as a useful quantity to explain hydrogen bonding, reactivity and structure–activity relationship of molecules and correlates with dipole moment, electronegativity, partial charges and site of chemical reactivity of the molecule. It provides a visual method to understand the relative polarity of a molecule. The regions with negative MEP corresponds to the areas of high electron density, representing a strong attraction between the proton and the points on the molecular surface, have the brightest red color and for the positive valued regions, areas of lowest electron density, have deep blue to indigo color, indicating the regions of maximum repulsion. The electron density isosurface onto which the electrostatic potential surface has been mapped is shown in Fig. 3 for CDMABA. The different values of the electrostatic potential at the surface are represented by different colors; red represents regions of most negative electrostatic potential, blue represents regions of most positive electrostatic po-

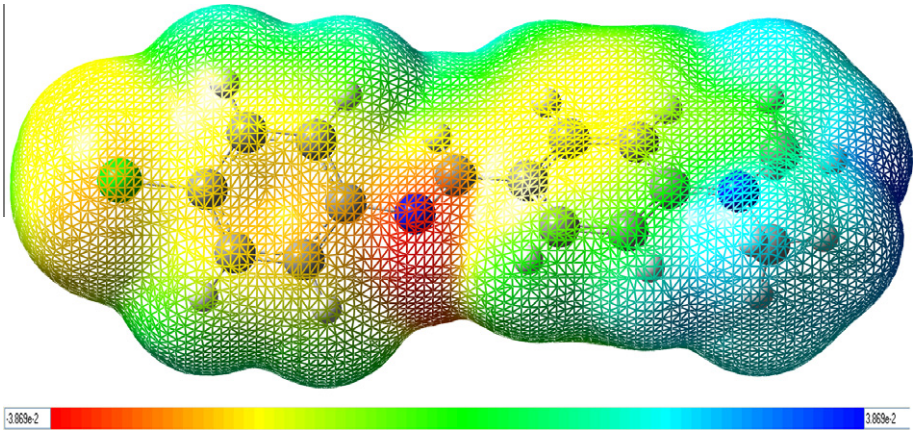

Fig. 3. Molecular electrostatic potential mapped on the isodensity surface in the range from −3.871e−2 (red) to +3.871e−2 (blue) for CDMABA calculated at the B3LYP/6-311++G(d,p) level of theory. (For interpretation of the references to color in this figure legend, the reader is referred to the web version of the article.)

Table 3
Theoretical and experimental vibrational wavenumbers (cm^{-1}) of CDMABA.

Unscaled	Scaled	Calculated (DFT)		Observed		Assignment (%PED, internal coordinates having contribution >5% are shown)
		IR intensities	Raman activities	FT-IR	FT-Raman	
3211	3071	0.7457	0.9489	3076	3069	Ph2[ν(CH)](98)
3210	3070	0.1086	11.7253	3076	3069	Ph2[ν(CH)](98)
3201	3062	0.3751	1.5302	3061	3069	Ph1[ν(CH)](98)
3198	3059	4.2381	1.7245	3061	3057	Ph1[ν(CH)](98)
3188	3050	0.5576	7.162	3045	3057	Ph2[ν(CH)](99)
3185	3047	3.9919	5.0902	3045	3057	Ph1[ν(CH)](99)
3179	3042	0.3646	2.0582	3045	3057	Ph1[ν(CH)](99)
3156	3021	2.3271	41.4374			Ph2[ν(CH)](97)
3134	3001	1.4028	35.5278	3009		Me2[ν(CH)](48) + Me1[ν(CH)](45)
3121	2989	1.1715	14.8167	3009		Me1[ν(CH)](51) + Me2[ν(CH)](47)
3051	2926	1.7417	14.708	2934		Me2[ν(CH)](95)
3047	2922	4.3875	10.8414	2934		Me1[ν(CH)](94)
2994	2874	2.3186	10.4817	2885		CH[ν(CH)](88) + CH[δ(CH)](10)
2990	2870	2.8194	28.3574	2868	2857	Me2[ν(CH)](68) + Me1[ν(CH)](24)
2983	2864	6.9956	41.6972	2868	2857	Me1[ν(CH)](72) + Me2[ν(CH)](26)
1679	1647	18.1239	0.4563	1639		ν(C=N)(58) + Ph2[ν(CC)](14)
1646	1616	1.5458	3.6348		1619	Ph2[ν(CC)](40) + Ph2[δ_{ring2}](8) + Ph1[ν(CC)](7) + ν(C=N)(6) + CH[ν(CC)](6)
1618	1589	1.0015	31.1296	1587	1598	Ph1[ν(CC)](47) + Ph1[δ_{ring1}](8) + ν(C=N)(7) + Ph1[δ(C4H) + δ(C7H) + δ(C6H)](12)
1598	1570	0.4358	11.1163		1578	Ph1[ν(CC)](67) + Ph1[δ_{ring1}](9) + Ph1[δ(C6H) + δ(C3H)](9)
1583	1556	6.411	18.1686	1560	1552	Ph2[ν(CC)](58) + Ph2[δ_{ring2}](8) + N(Me)2[δ(C18N)](6)
1559	1533	3.2177	1.5856	1539		Ph2[δ(C17H) + δ(C16H) + δ(C20H) + δ(C19H)](32) + Ph2[ν(CC)](25) + N(Me)2[ν(C18N)](18)
1531	1506	10.4026	0.2548	1493		Me2[δ_a(CH3)](40) + Me1[δ_a(CH3)](32)
1516	1491	9.0698	0.2968	1493		Me1[δ_a(CH3)](41) + Me2[δ_a(CH3)](36)
1512	1488	21.5082	17.1311		1484	Ph1[ν(CC)](33) + Ph1[δ(C3H)](15) + Ph1[δ(C7H)](14) + Ph1[δ(C6H)](14) + Ph1[δ(C4H)](10) + ν(C5N)(6)
1495	1471	6.8808	2.5345	1475		Me2[δ_a(CH3)](51) + Me1[δ_a(CH3)](39)
1488	1464	0.091	11.2136	1475		Me2[δ_s(CH3)](43) + Me1[δ_s(CH3)](36)
1486	1463	1.4533	2.3524	1475		Me1[δ_a(CH3)](51) + Me2[δ_a(CH3)](40)
1467	1444	19.816	8.2677	1447	1431	Ph2[ν(CC)](37) + Ph2[δ(C19H) + δ(C17H) + δ(C16H) + δ(C20H)](29) + Me1[δ_s(CH3)](12)
1447	1426	3.5429	1.9461	1416	1415	Me2[δ_s(CH3)](41) + Me1[δ_s(CH3)](40)
1431	1410	2.173	2.2302	1410	1409	Ph1[ν(CC)](43) + Ph1[δ(C4H) + δ(C7H) + δ(C6H) + δ(C3H)](35) + CH[δ(CH)](7)
1406	1386	23.916	79.2675		1404	CH[δ(CH)](54)
1384	1364	6.723	1.7269	1385	1366	N(Me)2[ν(C18N)](36) + Me2[ν(NC)](8) + N(Me)2[ρ(C18N)](7)
1362	1343	3.9522	57.9357			Ph2[ν(CC)](46) + Ph2[δ(C16H) + δ(C20H)](11) + N(Me)2[δ(C18N)](9) + N(Me)2[δ(C18N)](8) + Me1[ν(NC)](8)
1340	1323	25.8163	2.071	1325	1314	Ph2[δ(C17H) + δ(C16H) + δ(C20H) + δ(C19H)](37) + Ph2[ν(CC)](18) + CH[ρ(CH)](10) + CH[δ(CH)](9) + CH[ν(CC)](6)
1318	1301	26.1893	8.1864		1292	Ph1[δ(C6H) + δ(C3H) + δ(C4H) + δ(C7H)](81) + Ph1[ν(CC)](12)
1305	1289	38.7305	2.9045		1270	Ph1[ν(CC)](87)
1280	1264	15.1353	18.2776	1258	1252	CH[δ(CH)](22) + CH[ν(CC)](19) + ν(C5N)(13) + Ph2[ν(CC)](13) + Ph2[δ(C19H)](7) + Ph2[δ_{ring2}](6)
1264	1249	0.1829	16.8085	1246	1234	Ph2[ν(CC)](23) + Me2[ν(NC)](20) + Me1[ν(NC)](19) + Me1[ρ(CH3)](6)
1228	1214	0.2899	11.6829			ν(C5N)(26) + Ph2[δ((C17H)) + δ(C16H) + δ(C19H)](22) + Ph1[ν(CC)](9) + Ph1[δ_{ring1}](7)
1199	1186	29.8711	21.3708	1190	1202	Ph2[δ(C20H) + δ(C16H) + δ(C19H)](43) + Ph2[ν(CC)](9) + CH[ν(CC)](7)
1192	1179	0.1924	13.7569		1176	Ph1[δ(C7H) + δ(C6H) + δ(C4H) + δ(C3H)](21) + Me1[ρ(CH3)](19) + Me2[ρ(CH3)](18) + N(Me)2[ν(C18N)](8) + Ph2[ν(CC)](7)
1186	1174	0.4387	15.4857	1169	1163	Ph1[δ(C4H) + δ(C6H) + δ(C7H) + δ(C3H)](42) + ν(C5N)(9)
1149	1137	10.1544	206.0604	1134		Ph2[δ(C16H) + δ(C17H) + δ(C19H) + δ(C20H)](55) + Ph2[ν(CC)](28)
1138	1127	1.4197	0.1496		1123	Me2[ρ(CH3)](57) + Me1[ρ(CH3)](32)
1134	1122	27.9872	18.9524		1123	Me1[ρ(CH3)](60) + Me2[ρ(CH3)](32)
1126	1115	24.8763	1.3477	1107		Ph1[δ(C3H) + δ(C4H) + δ(C6H) + δ(C7H)](64) + Ph1[ν(CC)](27)
1097	1087	73.3568	104.0116	1092	1085	Ph1[ν(CC)](52) + Ph1[ν((CCl))](24) + Ph1[δ(C7H) + δ(C4H) + δ(C3H)](13) + Ph1[δ_{ring1}](7)
1079	1070	8.6452	3.6286	1074	1066	Me1[ρ(CH3)](31) + Me2[ρ(CH3)](31) + Me1[ν(NC)](15)+Me2[ν(NC)](15)
1024	1016	1.3928	2.7292	1013		Ph1[δ_{ring1}](59) + Ph1[ν(CC)](20)
1018	1010	57.9851	73.5207	1013		Ph2[δ_{ring2}](48) + Ph2[ν(CC)](37) + Ph2[δ(C19H) + δ(C17H)](7)
1005	998	14.7456	85.9241	989	1003	CH[ω(CH)](54) + Ph2[δ_{oop}(C16H) + δ_{oop}(C20H)](14) + τ(C13N)(12)
985	978	173.328	1181.451		981	Ph2[δ_{oop}(C16H) + δ_{oop}(C17H) + δ_{oop}(C20H)](82) + Ph2[τ_{ring2}](6)
973	966	64.042	8.9069		962	Ph1[δ_{oop}(C4H) + δ_{oop}(C3H) + δ_{oop}(C7H) + δ_{oop}(C6H)](89) + Ph1[τ_{ring1}](8)
961	954	145.805	763.7205	955		Me2[ν(NC)](26) + Me1[ν(NC)](26) + Ph2[ν(CC)](15) + Ph2[δ_{ring2}](7) + Me1[ρ(CH3)](6)
954	948	17.8097	530.4123		948	Ph1[δ_{oop}(C6H) + δ_{oop}(C7H) + δ_{oop}(C4H) + δ_{oop}(C3H)](68) + Ph1[τ_{ring1}](16) + Ph2[δ_{oop}(C20H)](6)
950	944	38.0106	32.3392		933	Ph2[δ_{oop}(C20H) + δ_{oop}(C19H)](65) + Ph2[τ_{ring2}](10)
897	892	2.5464	34.0415	897	886	CH[ρ(CH)](28) + δ(C=N)(12) + Ph2[ν(CC)](10) + CH[δ(CH)](8)
844	840	2.6601	15.9062	845		Ph1[δ_{oop}(C3H) + δ_{oop}(C4H) + δ_{oop}(C6H) + δ_{oop}(C7H)](42) + Ph1[ν(CC)](9) + Ph1[δ_{ring1}](9) + Ph1[τ_{ring1}](6) + δ_{oop}(C5N)(6)
843	839	1.3467	11.6108			Ph1[δ_{oop}(C3H) + δ_{oop}(C4H)](26) + CH[ν(CC)](6) + Ph2[ν(CC)](9) + Ph2[δ_{ring2}](8)
833	829	54.4441	125.8805	824	826	Ph2[δ_{oop}(C17H) + δ_{oop}(C16H) + δ_{oop}(C19H)](59) + N(Me)2[δ_{oop}(C18N)](13) + Ph2[τ_{ring2}](7)
823	819	13.0869	2.1912		818	Ph1[δ_{oop}(C6H) + δ_{oop}(C7H) + δ_{oop}(C3H) + δ_{oop}(C4H)](93)
810	807	400.5156	183.4457	806		Ph2[δ_{oop}(C19H) + δ_{oop}(C20H) + δ_{oop}(C17H) + δ_{oop}(C16H)](93)
749	746	5.1736	189.6042	791		Ph2[ν(CH)](13) + Ph2[δ_{ring2}](12) + CH[ρ(CH)](8) + Ph1[δ_{ring1}](7) + N(Me)2[ν(C18N)](6) + Me1[ν(NC)](6) + Ph2[τ_{ring2}](6) + Ph2[ν(CC)](6)

Table 3 (*continued*)

Unscaled	Scaled	Calculated (DFT)		Observed		Assignment (%PED, internal coordinates having contribution >5% are shown)
		IR intensities	Raman activities	FT-IR	FT-Raman	
743	740	9.4445	5.3129	743	736	Ph2[Puck](61) + N(Me)2[δ_{oop}(C18N)](13) + CH[δ_{oop}(CC)](11)
724	722	7.0857	81.3919	714	726	Ph1[Puck](60) + δ_{oop}(C5N)(12) + Ph1[δ_{oop}CCl)](9)
677	676	42.9502	233.6495	675	668	Ph1[δ_{ring1}](32) + Ph1[ν((CCl))](22)
651	650	2.0796	7.803			Ph2[δ_{ring2}](59) + Ph1[δ_{ring1}](15)
645	644	22.767	9.2079	642	632	Ph1[δ_{ring1}](62) + Ph2[δ_{ring2}](19)
563	563	16.1477	33.0679	561	567	Ph2[δ_{ring2}](21) + N(Me)2[ρ(C18N)](18) + Ph1[ν((CCl))](7)
544	544	160.0871	382.6117	542	548	Ph1[τ_{ring1}](23) + δ_{oop}(C5N)(13) + Ph1[δ_{oop}CCl)](13) + N(Me)2[δ_{oop}(C18N)](6)
534	534	14.6104	76.4237		535	N(Me)2[δ_{oop}(C18N)](18) + Ph2[τ_{ring2}](15) + CH[δ_{oop}(CC)](13)
503	503	51.0999	72.1068	511		Ph2[ν(CH)](14) + Ph1[τ_{ring1}](11) + N(Me)2[δ(C18N)](10) + Ph2[τ_{ring2}](8) + Ph1[δ_{oop}CCl)](7) + δ_{oop}(C5N)(7) + δ(C5N)(7)
470	471	250.883	156.1204	474	487	N(Me)2[δ(C18N)](38) + δ(C5N)(14)
456	456	121.2134	839.8383	461		N(Me)2[ρ(C18N)](37) + Ph1[ν((CCl))](17) + CH[ρ(CH)](6)
436	437	0.7658	163.6092	444	457	Ph2[τ_{ring2}](72) + Ph2[δ_{oop}(C19H) + δ_{oop}(C20H) + δ_{oop}(C17H)](14)
426	427	259.3662	6146.405	419	422	Ph1[τ_{ring1}](78) + Ph1[δ_{oop}(C6H) + δ_{oop}(C4H) + δ_{oop}(C7H) + δ_{oop}(C3H)](15)
399	400	615.351	2085.865	405		Ph2[τ_{ring2}](22) + Ph1[τ_{ring1}](15) + Ph1[δ_{oop}CCl)](14) + τ(C13N)(7) + CH[δ_{oop}(CC)](6) + Ph1[τ_{ring1}](8)
377	378	105.7516	2465.314		380	Ph1[δ_{ring1}](23) + Ph1[ν((CCl))](18) + Ph2[δ_{ring2}](16) + N(Me)2[ρ(C18N)](14) + N(Me)2[ν(C18N)](6)
347	348	81.4398	171.8293		351	CH[δ_{oop}(CC)](14) + δ(C5N)(13) + Ph1[δ(CCl)](11) + Ph2[τ_{ring2}](11) + Ph1[δ_{oop}CCl)](6)
313	314	128.2842	368.4551		318	Ph1[δ_{oop}CCl)](19) + Ph1[δ(CCl)](13) + N(Me)2[δ(C18N)](11) + CH[δ(CC)](9) + Ph1[τ_{ring1}](9) + δ_{oop}(C5N)(7)
273	274	38.8164	67.9053		278	Ph1[δCCl)](47) + N(Me)2[δ(C18N)](11) + N(Me)2[δ(C18N)](6)
250	251	30.5443	132.9871		245	Ph2[τ_{ring2}](25) + N(Me)2[δ_{oop}(C18N)](15) + Me1[τ(CH3)](11) + CH[τ(CC)](10) + τ(C5N)(6)
223	224	41.9127	114.0689		233	Me2[τ(CH3)](10) + N(Me)2[δ(C18N)](10) + δ(C5N)(8) + τ(C5N)(7) + Ph1[δ(CCl)](6) + CH[δ(CC)](6)
186	187	2.1685	3.1193		211	Me2[τ(CH3)](41) + Me1[τ(CH3)](15) + N(Me)2[δ(C18N)](15)
171	172	41.8165	250.6633			Ph1[τ_{ring1}](16) + δ(C=N)(12) + Ph1[δ_{oop}CCl)](9) + Ph2[δ_{ring2}](7) + τ(C5N)(7) + Ph1[δ_{ring1}](7) + CH[ν(CC)](6)
164	165	10.1857	58.1523			Me1[τ(CH3)](31) + Ph2[τ_{ring2}](13) + τ(C5N)(12) + CH[τ(CC)](10) + CH[δ_{oop}(CC)](8)
120	121	6.5133	30.8934			Ph1[τ_{ring1}](12) + CH[δ(CC)](11) + Ph2[τ_{ring2}](11) + Me2[τ(CH3)](10) + τ(C13N)(7) + CH[ρ(CH)](7)
91	92	2.6827	59.0938			Me2[τ(CH3)](25) + N(Me)2[δ_{oop}(C18N)](22) + Me1[τ(CH3)](12) + Ph2[τ_{ring2}](10)
76	77	0.9164	26.9178			N(Me)2[τ(C18N)](46) + Me1[τ(CH3)](30) + Me2[τ(CH3)](6)
68	69	4.7977	94.2586			N(Me)2[δ_{oop}(C18N)](42) + Me2[τ(CH3)](20) + Me1[τ(CH3)](16)
42	42	3.4486	203.4982			CH[ρ(CH)](18) + CH[τ(CC)](11) + δ(C=N)(11) + N(Me)2[δ_{oop}(C18N)](7) + Me2[τ(CH3)](7) + CH[δ(CC)](7) + CH[δ(CH)](7) + Ph1[τ_{ring1}](6) + N(Me)2[τ(C18N)](6)
35	35	10.6531	43.8939			τ(C5N)(35) + CH[τ(CC)](14) + δ(C5N)(10) + δ(C=N)(9) + CH[ρ(CH)](7) + N(Me)2[τ(C18N)](6) + CH[δ(CH)](6)
28	28	15.7108	186.0473			τ(C13N)(21) + N(Me)2[δ_{oop}(C18N)](16) + CH[δ_{oop}(CC)](14) + Me2[τ(CH3)](7) + Ph2[τ_{ring2}](7) + δ_{oop}(C5N)(6)

Types of vibration: ν, stretching; δ, deformation (bending), scissoring; δ_{oop}, out-of-plane bending; ω, wagging; ρ, rocking; τ, torsion; Puck, Puckering.

tential and green represents regions of zero potential. From Fig. 3, it is visible that the region of the most negative electrostatic potential is spread over the N12 atom of the central imine group. This indicates the delocalization of π electrons over the imine bridge nitrogen. This also reveals extended conjugation of the phenyl rings with the imine group.

4.5. Vibrational spectral analysis

The total number of atoms in this molecule is 33; hence, it gives 93 ($3n-6$) normal modes. The molecular conformation obtained from the crystalline structure, as well as the one yielded by geometry optimization, exhibits no special symmetries, and hence the molecule belongs to the C1 point group. As a consequence, all the 93 fundamental vibrations of the free molecule belong to the *A* irreducible representation and are both IR and Raman active. The vibrational spectral analysis have been carried out on the basis of FT-IR, FT-Raman spectra and the vibrational wavenumbers computed at B3LYP/6-311++G(d,p) level with their scaled wavenumbers. Vibrational mode assignments have been made on the basis of relative intensities, line shape, and potential energy distribution obtained from normal coordinate analysis. A good correlation was found between the computed and the experimental wavenumbers. The calculated vibrational wavenumbers, measured FT-IR and FT-Raman band positions and their calculated PED for each normal mode are presented in Table 3. The observed and calculated (scaled) infrared and Raman absorbance spectra are shown in Figs. 4 and 5, respectively. For the better understanding, vibrational modes have been discussed under separate heads viz. Phenyl ring vibrations, dimethyl amino group vibrations and imine group vibrations.

4.5.1. Phenyl ring vibrations

As far as the vibrational spectra are concerned, the benzene derivatives are the best recognized among the polyatomic systems. The observed phenyl ring vibrations are well reflected by DFT calculations and the assignments are made on the basis of potential energy distributions.

In the CDMABA molecule, the π-conjugated path comprises two phenyl rings PH2 and PH1 and the imine bridge. The phenyl ring PH2 and PH1 possess the *p*-substitutions. The selection rule for para-disubstituted phenyl ring allows four C–H stretching vibrations. Although the DFT predicts all these four bands, but these are observed as inseparable in IR. Usually Raman has one strong band in this zone [36]. The ring CH stretching vibrations appear to be very weak, which is due to steric interaction that induces effective conjugation and charge carrier localization resulting in twisted phenyl ring [37]. The very weak intense bands in IR at 3076, 3061 and 3045 cm^{-1} and the medium band in Raman at 3069 cm^{-1} with a shoulder at 3057 cm^{-1} are assigned to these modes and have been calculated in the range of 3071–3021 cm^{-1}.

The ring stretching vibrations are prominent in the vibrational spectra of benzene and its derivatives. There are five CC stretching vibrations associated with each phenyl ring which are more substituent dependent. Very strong peaks at 1587, 1560, 1539 and 1493 cm^{-1} in FT-IR and at 1619 1598, 1578 and1552 cm^{-1} in FT-Raman have been associated with CC stretching modes. DFT computation gives five vibrational modes of CC stretching with a contribution of ring bending and CH bending at 1589, 1570, 1410, 1289 and 1087 cm^{-1} for Ph1 ring and at 1616, 1556, 1533, 1444 and 1343 cm^{-1} for Ph2 ring. These modes of Ph2 ring are also having contributions from the vibrations of substituent dimethylamino group.

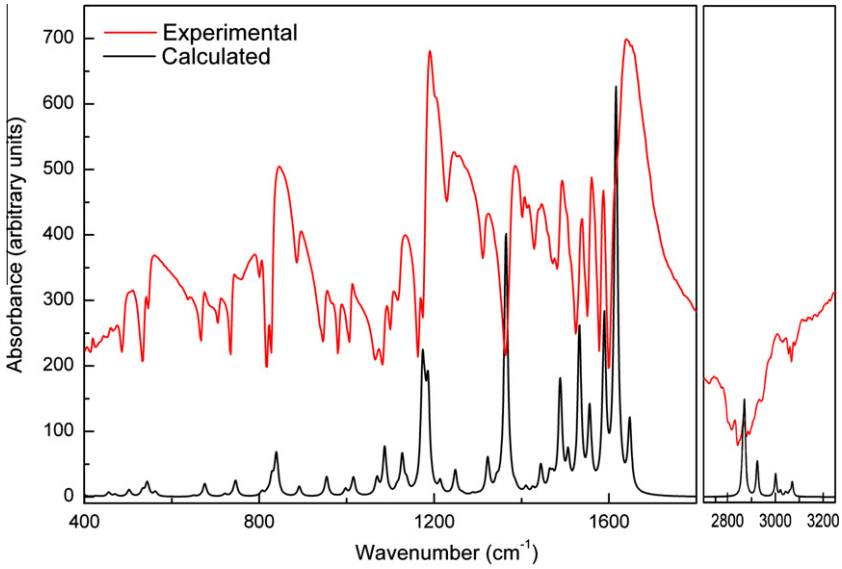

Fig. 4. Experimental and calculated infrared spectra of CDMABA.

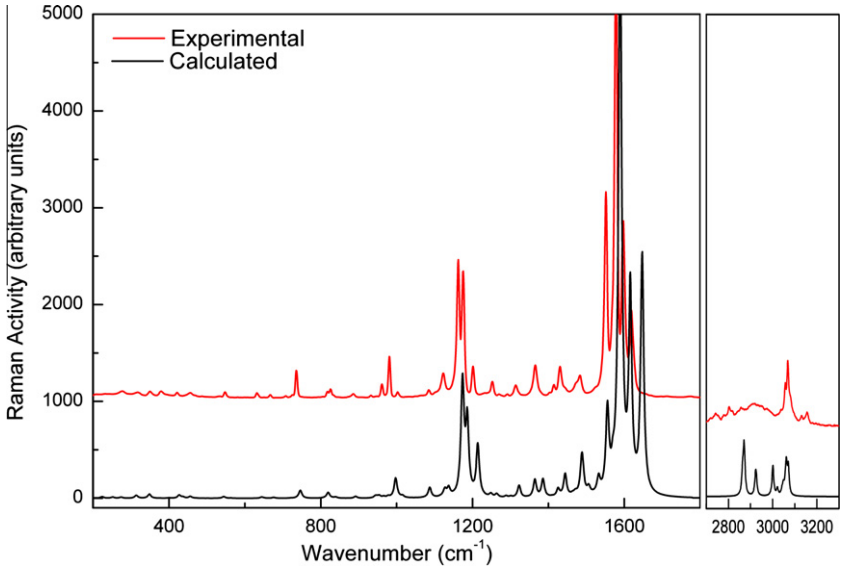

Fig. 5. Experimental and calculated Raman spectra of CDMABA.

The in-plane CH bending vibrations of the phenyl rings are found as a series of bands at 1325, 1190, 1169, 1134, 1107 cm^{-1}in FT-IR and their counterparts in FT-Raman are observed at 1314, 1202, 1163 and 1123 cm^{-1}. These modes are calculated at 1301, 1174, 1115 cm^{-1} and at 1323, 1186, 1137 cm^{-1} for Ph1 and Ph2, respectively. Computation of PED shows that these vibrations have coupling with CC stretching of the ring and the other vibrational modes of substituents.

The CH out-of-plane bending modes of the phenyl rings vibrate independently to give medium, strong and weak bands at 955, 845, 824 and 806 cm^{-1} in the IR but weak bands in the Raman spectrum at 981, 962, 948, 933, 826 and 818 cm^{-1}. These modes of vibrations have been calculated at 966, 948, 840 and 819 cm^{-1} for Ph1 and at 978, 944, 829 and 807 cm^{-1} for Ph2.

The observed strong and medium bands at 1013, 675, 642 and 561 cm^{-1} in FT-IR and very weak bands at 668, 632 and 567 cm^{-1} in FT-Raman and their computed values at around the same values are shown in Table 3 and are assigned to ring in-plane deformation modes. The ring puckering modes with a contribution of out-of-plane bending of the substituents are calculated at 722 and 740 cm^{-1} for Ph1 and Ph2, respectively and assigned to the bands at and 714, 743 and 726, 736 cm^{-1} in FT-IR and FT-Raman, respectively. Other fundamental modes of ring that show similar characteristics viz. torsional modes and their assignments have also been calculated and shown in Table 3 with their corresponding potential energy distributions.

4.5.2. Dimethylamino group vibrations

The important vibrational modes of this group are Ph–N stretch, N–$(CH_3)_2$ stretch and methyl deformations. The Ph–N stretching mode can be used as a good probe for evaluating bond configuration around the amino N atom and the electronic distribution of the aromatic amine compound. The observed peaks in IR at 1385 and in Raman at 1366 cm^{-1} are calculated at 1364 cm^{-1} and assigned to the Ph–N(C18–N) stretching with small contribution of N–Me stretch and N–$(CH_3)_2$ deformation. Similar assignments are also reported by Okamoto et al. [38]. The medium peaks observed at 1246 and 955 cm^{-1} in FT-IR spectra are

assigned to N–$(CH_3)_2$ stretching vibrations with a coupling of Ph2 ring CC stretching modes. Corresponding these modes weak peaks are observed at 1234 and 948 cm^{-1} in FT-Raman spectra. These modes calculated at 1249 and 954 cm^{-1}, respectively.

For the assignments of CH_3 group frequencies, several fundamental modes can be associated to each CH_3 group such as symmetric and asymmetric stretches, bends, and rock and torsional modes. Assignments of all these modes are given in Table 3. In the methyl group symmetric stretching modes $\nu_s(CH_3)$ are observed at 2868 cm^{-1} and 2857 cm^{-1} in FT-IR and FT-Raman spectra, respectively, and asymmetric stretching modes $\nu_a(CH_3)$ are observed at 3009 and 2934 cm^{-1} in the FT-IR spectra. A $\nu_s(CH_3)$ stretching mode are calculated to be 2870 and 2864 cm^{-1}, and $\nu_a(CH_3)$ asymmetric stretching modes are calculated to be 3001 and 2926 cm^{-1}. We have observed the asymmetric deformation modes $\delta_a(CH_3)$ at 1493 and 1475 cm^{-1} in the IR spectra and these modes are calculated at 1491 and 1471 cm^{-1}. The symmetric deformation $\delta_s(CH_3)$ modes are assigned to the observed peaks at 1416 cm^{-1} in the spectra and calculated at 1426 cm^{-1}.

The CH_3 rocking modes are assigned to weak Raman peaks at 1123 and 1066 cm^{-1} and the IR peaks at 1134 and 1074 cm^{-1} for the methyl groups. The calculated values of CH_3 rocking mode are obtained at 1127, 1122 and 1070 cm^{-1}. PED shows that the mode calculated at 1070 cm^{-1} is also having a major contribution from N–$(CH_3)_2$ stretching mode. The calculated wavenumber at 224, 187, 165 and 92 cm^{-1} shows a mixed contribution from CH_3 torsion around the N–C bond. The dimethylamino group provides more stabilization to the molecule and it is observed that characteristic bands fit reasonably well with the calculated wavenumbers.

4.5.3. Imine group vibrations

The vibrations of imine bridge are highly sensitive to the degree of charge transfer between the donor and acceptor groups, and therefore such stretching modes are of particular interest for spectroscopists. In imine group the C=N stretching bands are identified at 1639 cm^{-1} in IR spectra as a very strong intensity band because of the large change in dipole moment during this vibration. This mode is calculated at 1647 cm^{-1} with a mixed contribution of phenyl ring C=C stretching. The imine out-of-plane bending or in-plane wagging vibrations mainly mixed with other vibrational modes are computed in low frequency regions which can be barely observed in their FT-IR spectra. The imine C–H out-of-plane bending vibrations can be observed by weak peak at 989 cm^{-1} in FT-IR. The corresponding calculated mode has been found at 998 cm^{-1}. The imine C–H in-plane bending calculated at 1386 cm^{-1} is in excellent agreement with experimental assignments at 1385 and 1404 cm^{-1} in FT-IR and FT-Raman, respectively. Computations provide the torsional modes of imine group in low frequency region with a strong coupling of other group vibrational modes.

5. Conclusion

The calculated scaled wavenumbers using DFT employing 6-311++G(d,p) basis sets compares well with the experimental wavenumbers from Raman and IR spectra. A complete potential energy distribution (PED) indicates the composition of each normal mode in terms of internal coordinates, quantitatively assigning IR and Raman peaks in the fingerprint region. The natural bond orbital analysis (NBO) and MEP clearly shows delocalization of π and lone paired electrons of phenyl rings and nitrogen atoms, respectively. To the best of our knowledge this is the first study where a complete vibrational assignments with PED are reported along with NBO and MEP studies.

Acknowledgements

Authors would like to extend heartiest thanks to Dr. K. Ramamurthi of Crystal Growth and Thin Film Laboratory, School of Physics, Bharathidasan University, Tiruchirappalli 620 024, Tamil Nadu, India for providing sample. Financial assistance to Sapna Pathak from Jaypee University of Engg. & Technology, Guna is gratefully acknowledged.

References

[1] E.W. Van Stryland, H. Vanherzeele, M.A. Woodall, M.J. Soileau, A.L. Smirl, S. Guha, T.F. Bogess, Opt. Eng. 24 (1985) 613.
[2] M. Sheik-Bahae, A.A. Said, T. Wei, D.J. Hagan, E.W. Van Stryland, IEEE J. Quantum Electron. 26 (1990) 760.
[3] J.J. Rodrigues Jr., L. Misoguti, F.D.C.R. Nunes Mendonca, S.C. Zilio, Opt. Mater. 22 (2003) 235.
[4] M. Somac, A. Somac, B.L. Davies, M.G. Humphery, M.S. Wong, Opt. Mater. 21 (2002) 485.
[5] L.V. Natarajan, R.L. Sutherland, V.P. Tondiaglia, T.J. Bunning, W.W. Adams, J. Nonlinear Opt. Phys. Mater. 5 (1996) 89.
[6] X. Xu, W. Qiu, Q. Zhou, J. Tang, F. Yang, Z. Sun, P. Audebert, J. Phys. Chem. B 112 (16) (2008) 4913.
[7] J.G. Breitzar, D.D. Diott, L.K. Iwaki, S.M. Kirkpatrick, T.B. Rauchturs, J. Phys. Chem. A 103 (1999) 6930.
[8] A. Karakaş, A. Elmali, H. Ünver, I. Svoboda, Spectrochim. Acta Part A 61 (2005) 2979.
[9] W. Yu, L. Yang, T.L. Zhang, J.G. Zhang, F.J. Ren, Y.H. Liu, R.F. Wu, J.Y. Guo, J. Mol. Struct. 794 (2006) 255.
[10] K. Srinivasan, R. Biravaganesh, R. Gandhimathi, P. Ramasamy, J. Cryst. Growth 236 (2002) 381.
[11] N. Azariah, A.S.H. Hameed, T. Thennappan, M. Noel, G. Ravi, Mater. Chem. Phys. 88 (2004) 90.
[12] S. Leela, K. Ramamurthi, H.S. Evans, G. Vasuki, Acta Crystallogr. E 63 (2007) O4805.
[13] X.L. You, C.R. Lu, Y. Zhang, D.C. Zhang, Acta Crystallogr. C 60 (2004) O693.
[14] Y. Dmezawa, Bull. Chem. Soc. Jpn. 71 (1998) 1207.
[15] C.V.K. Sharma, J. Chem. Soc. Perkin Trans. 2 (1993) 2209.
[16] S. Leela, K. Ramamurthi, G. Bhagvannarayana, Spectrochim. Acta Part A 74 (2009) 78.
[17] P. Hohenberg, W. Kohn, Phys. Rev. B 864 (1964) 136.
[18] M.J. Frisch, G.W. Trucks, H.B. Schlegel, G.E. Scuseria, M.A. Robb, J.R. Cheeseman, J.A. Montgomery, T. Vreven, K.N. Kudin, J.C. Burant, J.M. Millam, S.S. Iyengar, J. Tomasi, V. Barone, B. Mennucci, M. Cossi, G. Scalmani, N. Rega, G.A. Petersson, H. Nakatsuji, M. Hada, M. Ehara, K. Toyota, R. Fukuda, J. Hasegawa, M. Ishida, Nakajima, Y. Honda, O. Kitao, H. Nakai, M. Klene, X. Li, J.E. Knox, H.P. Hratchian, J.B. Cross, C. Adamo, J. Jaramillo, R. Gomperts, R.E. Stratmann, O. Yazyev, A.J. Austin, R. Cammi, C. Pomelli, J.W. Ochterski, P.Y. Ayala, K. Morokuma, G.A. Voth, P. Salvadorm, J.J. Dannenberg, V.G. Zakrzewski, S. Dapprich, A.D. Daniels, M. C.Strain, O. Farkas, D.K. Malick, A.D. Rabuck, K. Raghavachari, J.B. Foresman, J.V. Ortiz, Q. Cui, A.G. Baboul, S. Clifford, J. Cioslowski, B. Stefanov, G. Liu, A. Liashenko, P. Piskorz, I. Komaromi, R.L. Martin, D.J. Fox, T. Keith, M.A. Al-Laham, C.Y. Peng, A. Nanayakkara, M. Challacombe, P.M.W. Gill, B. Johnson, W. Chen, M.W. Wong, C. Gonzalez, J.A. Pople, Gaussian 03, Revision C.02, Gaussian Inc., Wallingford, CT 06492, 2003.
[19] C.T. Lee, W.T. Yang, R.G. Parr, Phys. Rev. B 37 (1988) 785.
[20] R.G. Parr, W. Yang, Density Functional Theory of Atoms and Molecules, Oxford University Press, New York, 1989.
[21] A.D. Becke, J. Chem. Phys. 98 (1993) 5648;
Mantzaris, J. Chem. Phys. 89 (1988) 2193.
[22] P. Pulay, G. Fogarasi, F. Pang, J.E. Boggs, J. Am. Chem. Soc. 101 (1979) 2550.
[23] G. Fogarasi, X. Zhou, P.W. Taylor, P. Pulay, J. Am. Chem. Soc. 114 (1992) 8191.
[24] J.M.L Martin, C. Van Alsenoy, Gar2ped, University of Antwerp, 1995.
[25] G.A. Zhurko, D.A. Zhurko, Chemcraft, 2005, <http://www.chemcraftprog.com>.
[26] H. Yoshida, K. Takeda, J. Okamura, A. Ehara, H. Matsurra, J. Phys. Chem. A 106 (2002) 3580.
[27] A.E. Reed, L.A. Curtiss, F. Weinhold, Chem. Rev. 88 (1988) 899.
[28] J. Chocholousova, V. Vladimir Spirko, P. Hobza, Phys. Chem. Chem. Phys. 6 (2004) 37.
[29] L.H. Ma, Z.B. Chen, Y.B. Jiang, Chem. Phys. Lett. 372 (2003) 104.
[30] C.M. Whitaker, E.V. Patterson, K.L. Kott, R.J. McMahon, J. Am. Chem. Soc. 118 (1996) 9966.
[31] Z.G. Liu, H. Nazare, Synth. Met. 111 (2000) 47.
[32] A. Yamamori, C. Adachi, T. Koyama, Y. Taniguchi, J. Appl. Phys. 86 (1999) 4369.
[33] D. Kolosov, V. Adamovich, P. Djurovich, M.E. Thompson, C. Adachi, J. Am. Chem. Soc. 124 (2002) 9945.
[34] C. James, G.R. Pettit, O.F. Nielsen, V.S. Jayakumar, I. Hubert Joe, Spectrochim. Acta 70A (2008) 1208.
[35] P. Politzer, D.G. Truhlar (Eds.), Chemical Applications of Atomic and Molecular Electrostatic Potentials, Plenum Press, New York, 1981.
[36] F.R. Dollish, W.G. Fateley, F.F. Bentley, Characteristic Raman Frequencies of Organic Compounds, Wiley, New York, 1974.
[37] H. Neugebauer, C. Kvarnstrom, C. Brabec, N.S. Sariciftci, R. Kiebooms, F. Wudl, S. Luzzati, J. Chem. Phys. 110 (12) (1999) 108.
[38] H. Okamoto, H. Inishi, Y. Nakamura, S. Kohtani, R. Nakagaki, Chem. Phys. 260 (2000) 193.